4.1. Introduction

As discussed in Chapter 1, the ideal ABO_3 perovskite structure has cubic symmetry with $Pm\bar{3}m$ space group [Mitchell (2002)]. The attractiveness of the perovskite structure is that it can house a diversity of ions at A and B-sites with dissimilar valance and ionic sizes leading to extensively unusual physical properties [Mitchell (2002)]. Putting cations having different ionic valence together at A-site leads to mixed valence perovskites. Doping of tetravalent cation like Ti^{4+} at Mn-site in mixed valence manganites leads to interesting structural and magnetic properties due to modification in bond lengths and bond angles. Since the ionic radius of the Ti^{4+} (r = 0.605 Å) ion is known to lie in between those of Mn^{4+} (r = 0.530 Å) and Mn^{3+} (r = 0.645 Å) and the available literature on Ti-doped manganites signify that Ti^{4+} ions replace the isovalent Mn^{4+} ions in these materials [Shang et al. (2014); Shannon (1976)], but there may exist another possibility that a fraction of Ti^{4+} ions substitute for Mn^{3+} ions, leading to oxygen non-stoichiometry [Kulkarni et al. (2008)]. Recently, however, it has been reported that at higher doping levels Ti^{4+} ions engage Mn^{3+} sites in addition to Mn^{4+} sites resulting of Mn^{2+} ions [Zhu et al. (2006)].

One of the most significant issues in magnetic nanoparticles consisting of an antiferromagnetic (AFM) component is the finite-size effect. As an AFM component generally has two mutually compensating sublattices, at the surface there is always breaking of the sublattice pairing, and it leads to uncompensated surface spins. As the size of magnetic nanoparticle system decreases, the importance of the uncompensated surface spins increases; this can additionally lead to unusual magnetic properties, such as coercivities and hysteresis loop shifts, significant magnetic moments, spin-glass (SG) or cluster-glass-like behavior of the surface spins [Zhang et al. (2010)]. The SG is a system where there is a lack of long-range magnetic ordering. It initiates from the

frustration of spins, disorders or mixed interactions having both ferromagnetic (FM) and AFM interactions. In a process, where few FM interactions get changed to AFM, the phase would still be FM but with some moments receiving disturbances. If the existence of random AFM interactions increases beyond a threshold, frustration increases and long-range FM ordering is hindered, this, in turn, favors a spin glass phase. Some materials reenter into an inhomogeneous state while cooling from a homogeneous state. When such a kind of transition exists, i.e., from FM/AFM to SG, where SG exists in lower temperatures, the system is a reentrant spin glass (RSG) [Viswanathan et al. (2009)]. Interestingly, the RSG has also been reported in several other systems such as orthoferrites [Xavier Jr. et al. (2004)], nickel doped perovskites [Viswanathan et al. (2009); Moreno et al. (2007)], orthochromites [Manna et al. (2013)], intermetallic compounds [Gao et al. (2012); Grover et al. (1988)] and double perovskites [Ghara et al. (2014)].

Interestingly, mixed-valence manganites also exhibit quite exciting dielectric property. Munoz et al. (2009) and Thakur et al. (2013) studied dielectric behavior for the strontium-doped bismuth manganites ($Bi_{1-x}Sr_xMnO_3$ = BSMO) separately. They reported very high dielectric constant of the order of ~10^6 arising mainly due to orientational polarization. Thakur et al. found that the value of dielectric constant for BSMO increases with increasing Sr^{2+}-ion at Bi-site from ~10^2 (very low) for x = 0.40 to ~10^6 (very high) for x = 0.45 and slightly decreases to ~10^5 for x = 0.55 with further increasing concentration of Sr^{2+}-ion [Thakur et al. (2013)].

In this chapter, we have investigated the structural and magnetic properties of newly synthesized microflakes and microrods of $Nd_{0.7}Ba_{0.3}Mn_{1-x}Ti_xO_3$ (NBMTO) manganites with x = 0.40 and 0.50. Structural analysis was performed by Rietveld refinement which reveals the coexistence of two crystallographic phases with *I*4*/mcm*

and *P*4*mm* space groups. Temperature-dependent magnetization measurements show that both samples undergo PM to FM phase transition. Frequency-dependent ac susceptibility measurements reveal that these samples are showing RSG behavior. To the best of our knowledge, among the existing oxide RSG systems, NBMTO has the lowest difference between the ferromagnetic transition temperature (T_C) and spin glass freezing temperature (T_f). With different magnetic measurements, such as ac and dc magnetizations, we suggest the presence of RSG nature in NBMTO with T_C = 30.64 K and T_f = 23.50 K for x = 0.40 and T_C = 20.17 K and T_f = 15.26 K for x = 0.50. Frequency and temperature dependence of dielectric response, electrical resistivity, and conductivity along with dielectric loss were studied by Impedance Analyzer in the frequency range from 100 Hz to 1 MHz.

4.2. Experimental Details

The polycrystalline samples of $Nd_{0.7}Ba_{0.3}Mn_{1-x}Ti_xO_3$ manganites with x = 0.40 and 0.50 were synthesized by using auto-combustion technique [Kumar et al. (2019] as described in Chapter 2. The obtained brownish-black powder after combustion was grinded and the sample with x = 0.50 was calcined at 1200 & 1300°C, and finally both samples were calcined at 1350°C for 6 hrs in a programmable furnace. The X-ray diffraction (XRD) pattern of calcined powders were recorded using Rigaku, Miniflex600 X-ray diffractometer having Cu target as an X-ray source in the 2θ range of 20°-120° with a scan rate of 2°/min. The structural analysis was done using Rietveld refinement of the XRD patterns with the help of FullProf Suite [Carvajal (1993)]. The microstructural and compositional/elemental studies were done using High-Resolution Scanning Electron Microscopy (HR-SEM) and Energy-Dispersive X-ray spectroscopy (EDS) available in the same system (FEI, Nova NanoSEM 450), respectively. The magnetic properties of the samples were measured using SQUID, vibrating sample

magnetometer (VSM), magnetic property measurement system (MPMS3: Quantum Design Inc., USA) as described in Chapter 2. The relative dielectric permittivity (dielectric constant), dielectric loss, electrical conductivity and resistivity of the synthesized samples were measured by making parallel plate capacitor using Impedance Analyzer (E4990A, Keysight Technologies) at the frequency range 100 Hz to 1 MHz from 25°C (298 K) to 300°C (573 K). The parallel plate capacitor of the samples for the dielectric measurements was prepared by making pellets of the calcined samples and sintering at 1350°C for 3 hrs for the densification of the samples. The surfaces of the pellets were coated with silver paste and fired at 300°C for one hr to ensure the electrical contact with the electrodes.

4.3. Results and Discussion

4.3.1. Microstructural and Crystal Structure Analysis

4.3.1.1. Morphological and Elemental Analysis

Figs. 4.1(a-b) and **4.1**(c-d) show the HR-SEM micrographs of powder samples for $Nd_{0.7}Ba_{0.3}Mn_{1-x}Ti_xO_3$ with x = 0.40 and 0.50, respectively. Both the samples show two different types of morphologies in two different regions. The sample with x = 0.40 grown in grain forms with grain size lying in the range 250-775 nm and micro-flake like structure with length ranging 10-30 μm and a width ranging 1-5 μm. In contrast, the sample with x = 0.50 grown into micro-rods with circular and rectangular cross-sections and rod length ranging in 2-10 μm and diameter of 0.5-1.0 μm and shows grains in the range 500-1000 nm. The significance of these systems is that these are grown into specified shapes, which is generally not observed by combustion synthesis method. To the best of our knowledge, no such microstructures were detected in the other manganite systems using the current method. **Figs. 4.1**(e-f) and **4.1**(g-h) show the EDS spectra of $Nd_{0.7}Ba_{0.3}Mn_{1-x}Ti_xO_3$ with x = 0.40 and 0.50, respectively, corresponding to their

respective micrographs. The characteristic peaks corresponding to Nd, Ba, Mn, Ti, and O in the EDS spectra show the presence of Nd, Ba, Mn, Ti and O in the samples. As we know that technique of EDS is not suitable for the quantitative analysis of lighter atoms like “oxygen” which does not give the correct composition, therefore, we performed the quantitative analysis of the nominal composition by excluding “oxygen” atoms. The quantitative analysis for both the samples and for both the micrographs of each sample was performed and is found that there is redistribution of elements than the nominal composition in the different microstructures within the samples. The redistribution of elements is mainly seen for the Ti and Mn occupying the B-sites. Hence, the occurrence of two different microstructures within the same sample is due difference in grain growth mechanisms for different elemental compositions. The compositional redistribution in metallurgical and ceramic solid solutions with limited solid solubility is well known in literature [Barsoum (2000); Reed-Hill (1964)]. In such systems, the compositions of coexisting phases correspond to the minima in Gibb’s free energy. Changing the composition of the solid solution system only changes the phase fraction of the two components in phase coexistence region. More studies will be needed to draw the conclusive evidences for such phase coexistence in the present system. Since it is not possible for us to separate out physically the two types of microstructural region of the samples, the crystallographic, dielectric and magnetic characterizations were performed on the as prepared samples having both types of microstructures. This $Nd_{0.7}Ba_{0.3}Mn_{1-x}Ti_xO_3$ with x = 0.40 and 0.50 needs to be investigated in more detail in future to settle out various subtle features of this system.

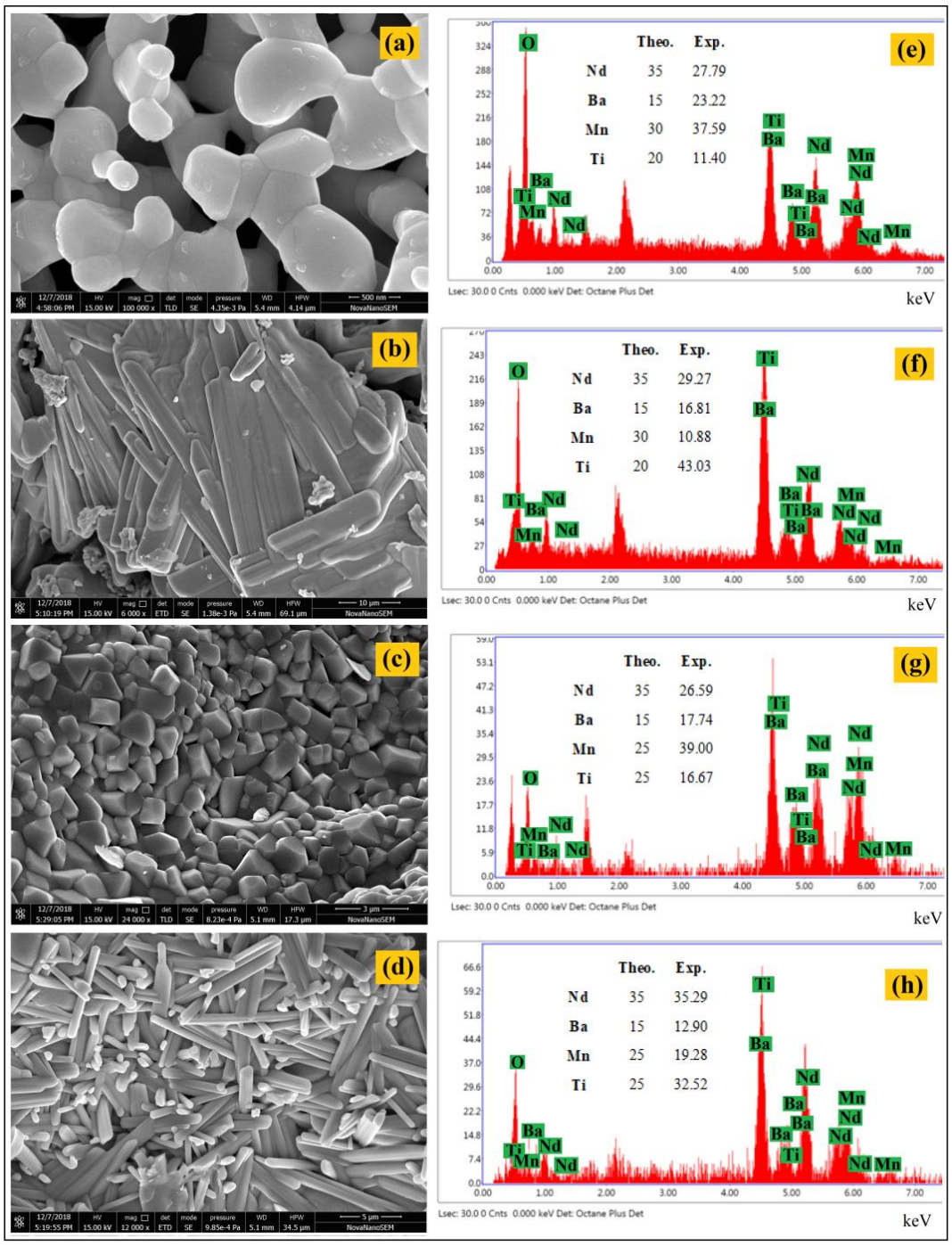

Figure 4.1: HR-SEM micrographs of $Nd_{0.7}Ba_{0.3}Mn_{1-x}Ti_xO_3$ manganites for (a-b) x = 0.40 and (c-d) x = 0.50 taken into two different regions. The energy dispersive X-ray spectroscopy (EDS) spectra of $Nd_{0.7}Ba_{0.3}Mn_{1-x}Ti_xO_3$ for (e-f) x = 0.40 and (g-h) x = 0.50 showing presence of elements in nominal compositions.

4.3.1.2. Structural Analysis: Rietveld Refinement

Room temperature X-ray diffraction (XRD) pattern for $Nd_{0.7}Ba_{0.3}Mn_{1-x}Ti_xO_3$ manganite with x = 0.50 calcined at different temperatures i.e. 1200, 1300 and 1350°C for 6hrs are shown in **Fig. 4.2**(a) in the 2θ range 20°-120°. At lower calcination temperatures there are small amount of impurity phases of $BaMnO_3$ and Mn_3O_4 which reduce with increasing calcination temperature and results in negligible impurity phase at 1350°C. As discussed in Chapter 3, there is coexistence of two crystallographic phases in $Nd_{0.7}Ba_{0.3}Mn_{1-x}Ti_xO_3$ for $x \geq 0.30$. For $x \leq 0.30$ no impurity phase was observed in room temperature XRD pattern, as reported by us [Kumar et al. (2019)] and discussed in Chapter 3. Substitution of larger concentration of Ti^{4+}-ion at Mn-site makes the perovskite structure less stable when it starts substituting Mn^{3+} sites and consequently impurity phase appear. **Fig. 4.2**(b) shows room temperature XRD patterns for $Nd_{0.7}Ba_{0.3}Mn_{1-x}Ti_xO_3$ with x = 0.40 and 0.50 calcined at 1350°C**.** The inset of **Fig. 4.2(b)** shows the selected XRD patterns between 2θ = 39°-41° containing $(112)_B/(200)_B$ plane reflection(s) from body centered tetragonal structure and $(110)_P$ plane reflection due to the primitive tetragonal crystal structure. The orthorhombic $(112)_B/(200)_B$ plane reflections get shifted towards lower angle side on doping of Ti^{4+} ions resulting in to increased unit cell volume due to replacement of Mn^{4+} (0.530 Å) ions by Ti^{4+} (0.605 Å) ions. The tetragonal $(110)_P$ plane reflections get shifted towards higher angle side due to replacement of Mn^{3+} (0.645 Å) ions by Ti^{4+} (0.605 Å) ions which results in to decrease in unit cell volume. The Rietveld fits for the XRD patterns of $Nd_{0.7}Ba_{0.3}Mn_{1-x}Ti_xO_3$ manganites with x = 0.40 and 0.50 are shown in **Figs. 4.3(a-b)**. The Rietveld refinement of the structure confirms the coexistence of two crystallographic phases of tetragonal structure with *I*4*/mcm* and *P*4*mm* space groups.

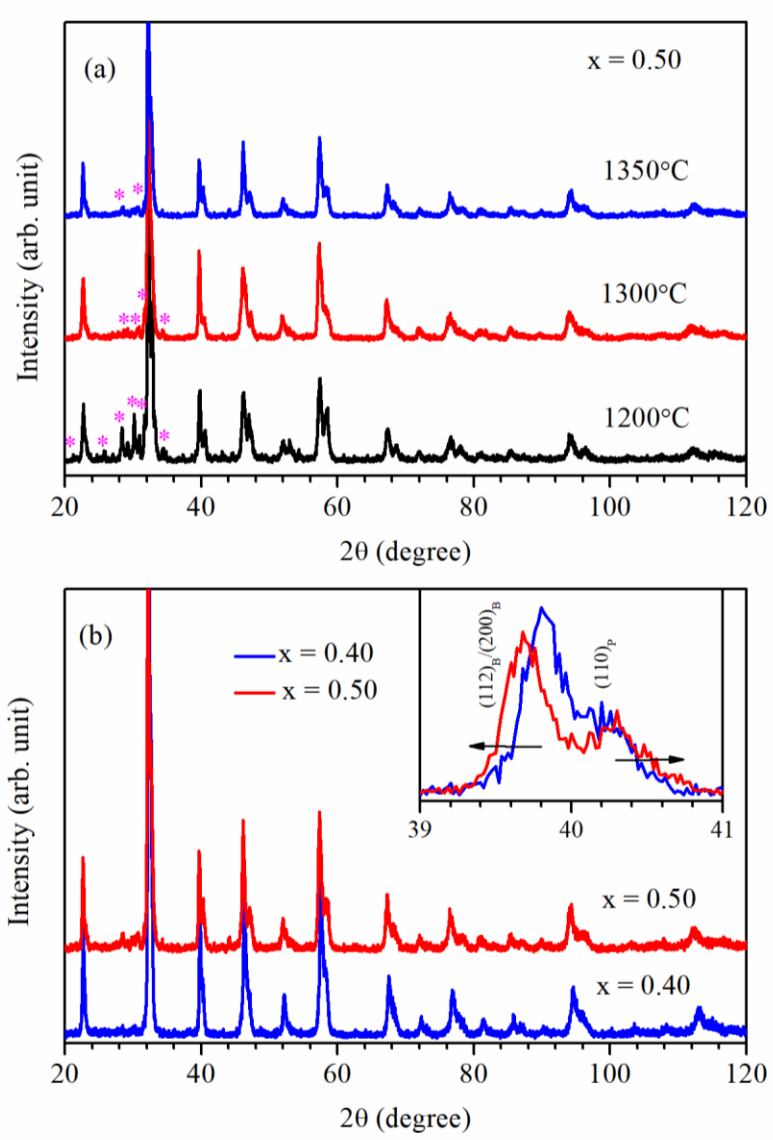

Figure 4.2: (a) Room temperature XRD patterns for $Nd_{0.7}Ba_{0.3}Mn_{1-x}Ti_xO_3$ manganite with x = 0.50 calcined at 1200, 1300 and 1350°C in the 2θ range 20º-120º; the asterisk (*) show the impurity peaks of $BaMnO_3$ and Mn_3O_4. (b) Room temperature XRD patterns for $Nd_{0.7}Ba_{0.3}Mn_{1-x}Ti_xO_3$ manganites with x = 0.40 and 0.50 calcined at 1350°C. The inset of (b) shows selected XRD profile between 39°-41° showing that peak(s) $(112)_B/(200)_B$ shifting towards lower angle side and peak $(110)_T$ towards higher angle side.

As reported by Zhu et al. (2006) in another system for $La_{0.7}Sr_{0.3}Mn_{1-x}Ti_xO_3$ lattice parameter for pseudocubic structure increases from 3.872 Å (x = 0) to 3.892 Å (x = 0.30) due to replacement of Mn^{4+} (0.530 Å) by Ti^{4+} (0.605 Å) for $x \leq 0.30$, and decreases from 3.892 Å (x = 0.30) to 3.883 Å (x = 0.50) for $x \geq 0.30$ due to replacement of Mn^{3+} (0.645 Å) by Ti^{4+} (0.605 Å). Here, in our case, for $Nd_{0.7}Ba_{0.3}Mn_{1-x}Ti_xO_3$ system, the unit cell volume for body centered orthorhombic/tetragonal structure increases from 235.10(5) $Å^3$ to 242.20(4) $Å^3$ while changing the composition from x = 0 to x = 0.3 due to substitution of Mn^{4+}-ions by Ti^{4+}-ions. In the compositions with x > 0.30, the unit cell volume increases from 241.46(4) $Å^3$ to 243.40(5) $Å^3$ while changing the composition from x = 0.40 to x = 0.50 for body centered tetragonal structure with *I*4/*mcm* space group. But for the primitive tetragonal structure with *P*4*mm* space group unit cell volume decreases from 58.97(3) $Å^3$ for x = 0.30 to 58.34(3) $Å^3$ for x = 0.50. This suggests that for the same composition (x = 0.30), the body centered tetragonal structure with *I*4/*mcm* space group is favoring substitution of Mn^{4+} by Ti^{4+}-ions while primitive tetragonal structure with *P*4*mm* space group is favoring Mn^{3+} substitution by Ti^{4+}-ions. The enhancement of the unit cell volume for *I*4/*mcm* space group is also governed by the formation of Mn^{2+} ions to maintain the charge neutrality for x < 0.30. The detailed results obtained from Rietveld structure refinements are listed in **Table 4.1**. The Rietveld fits for the $Nd_{0.7}Ba_{0.3}Mn_{1-x}Ti_xO_3$ perovskite manganites with x = 0.40, 0.50 are shown in **Figs. 4.3**(a-b), respectively. In this figure, dots indicate the experimental data and the calculated data is the continuous line. The lowest curve shows the difference between experimental and calculated patterns. The vertical bars indicate the expected Bragg's reflection positions. **Figs. 4.3**(c-d) represent the schematic ball and stick unit cell model for the sample with x = 0.40 for space groups *I*4/*mcm* and *P*4*mm*, respectively.

Table 4.1: Refined lattice parameters, unit cell volume and χ^2 for *P4mm* and *I4/mcm* phases of $Nd_{0.7}Ba_{0.3}Mn_{1-x}Ti_xO_3$ manganites with x = 0.30, 0.40 and 0.50 obtained from Rietveld structure refinement.

Parameters	**x = 0.30**		**x = 0.40**		**x = 0.50**	
	I4/mcm	***P4mm***	***I4/mcm***	***P4mm***	***I4/mcm***	***P4mm***
a (Å)	5.5426(5)	3.888(2)	5.5486(5)	3.8968(7)	5.5612(4)	3.8931(7)
c (Å)	7.8442(5)	3.901(2)	7.8427(8)	3.8588(7)	7.870(1)	3.8560(9)
V (Å^3)	242.20(4)	58.97(6)	241.46(4)	58.60(2)	243.40(5)	58.44(2)
χ^2	1.48		1.43		1.60	

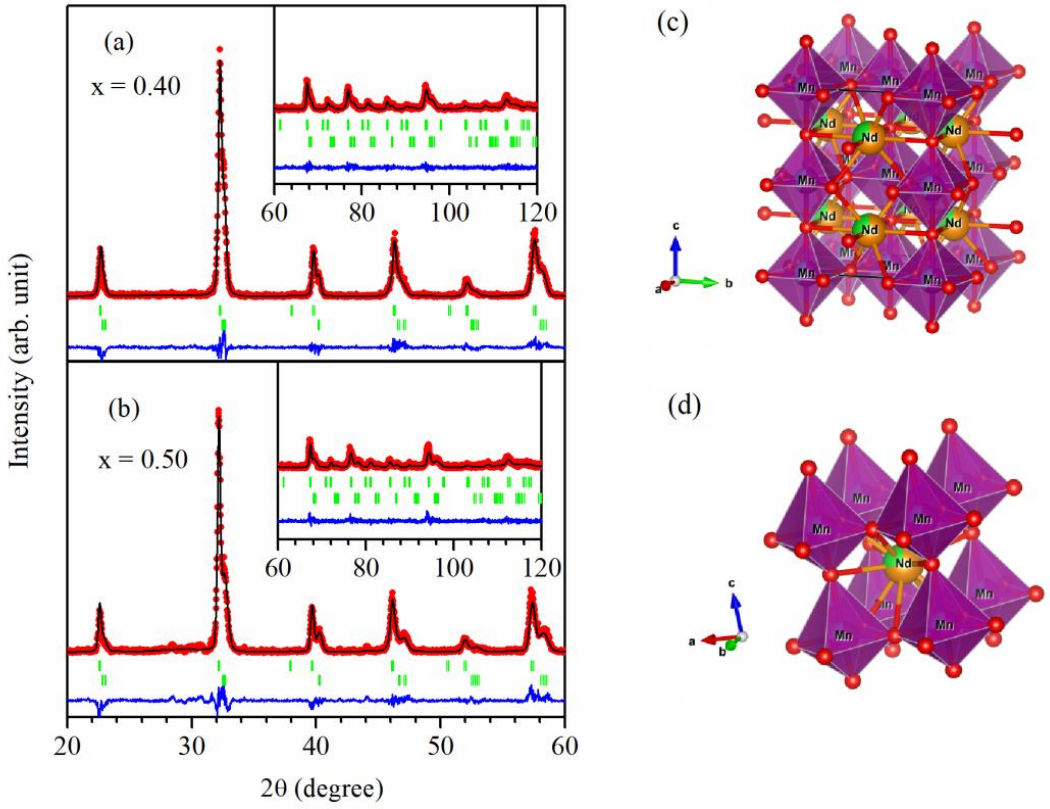

Figure 4.3: Rietveld fits for the XRD patterns of $Nd_{0.7}Ba_{0.3}Mn_{1-x}Ti_xO_3$ compounds, (a) x = 0.40 and (b) 0.50. Dots indicate the experimental data and the calculated data is the continuous curve, overlapping them. The lowest curve shows the difference between experimental and calculated XRD patterns. The vertical bars indicate the expected Bragg's reflection positions. The upper vertical bars indicate the Bragg's position for *I4/mcm*, while lower for *P4mm*. (c) and (d) Ball and Stick models for the unit cell of *I4/mcm* and *P4mm* space groups for the sample with x = 0.40, respectively.

Fig. 4.4 depicts the structural phase diagram for $Nd_{0.7}Ba_{0.3}Mn_{1-x}Ti_xO_3$ (NBMTO) manganites for the composition range $0 \leq x \leq 0.50$. **Fig. 4.4** clearly shows that for $x < 0.30$, NBMTO crystallize into a single phase orthorhombic structure with *Imma* space group and for $x \geq 0.30$ it exhibits coexistence of two tetragonal phases with *I4/mcm* and *P4mm* space groups. Further, for $x \leq 0.30$, the unit cell volume increases with increasing concentration of Ti^{4+}-ions due to replacement of Mn^{4+}-ions by Ti^{4+}-ions. For $x \geq 0.30$, the unit cell volume for *P4mm* space group decreases with increasing Ti^{4+}-ions due to replacement of Mn^{3+}-ions, and due to charge neutrality another Mn^{2+}-ion (0.83 Å) is generated causing enhancement in unit cell volume in orthorhombic *I4/mcm* space group [Shannon (1976)].

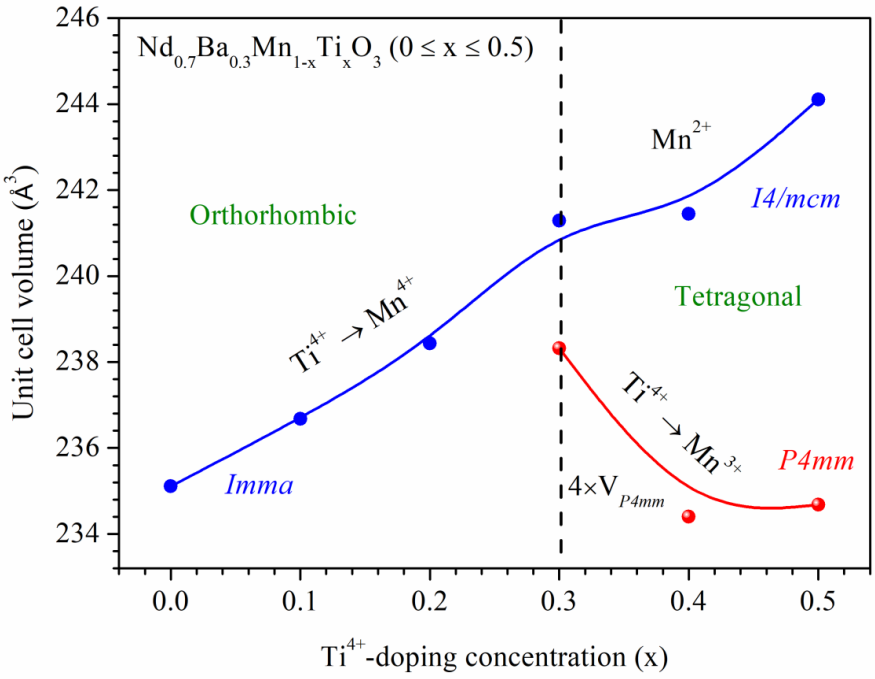

Figure 4.4: Structural phase diagram for $Nd_{0.7}Ba_{0.3}Mn_{1-x}Ti_xO_3$ ($0 \leq x \leq 0.50$) manganites.

4.3.2. Magnetic Properties

4.3.2.1. Temperature Dependent Magnetization Studies

The temperature dependent magnetizations M(T) curves of $Nd_{0.7}Ba_{0.3}Mn_{1-x}Ti_xO_3$ manganites with x = 0.40 and 0.50 are shown in **Fig. 4.5**(a), measured in zero field cooled (ZFC) and field cooled (FC) conditions at a constant field of H = 200 Oe in the temperature range 2 K ≤ x ≤ 370 K. During ZFC magnetization M_{ZFC} measurement the sample was first cooled from room temperature to 2 K without application of magnetic field and measured magnetization under applied field while during FC magnetization M_{FC} measurement the sample was cooled from room temperature to 2 K under application of magnetic field and the magnetization was measured under an applied field of 200 Oe from 2 K to 370 K. The FC and ZFC magnetizations show significant difference at low temperatures and a broad hump is observed in M_{ZFC} curve. The inset of **Fig. 4.5(a)** displays low-temperature zoomed portion of M_{ZFC} and M_{FC} curves for the sample with x = 0.40, which shows three different anomalies (~22 K, ~10 K & ~2.3 K) in low-temperature region as marked by arrows which correspond to various magnetic transition. A similar magnetic behavior is also observed for x = 0.50. At lower temperatures the M_{FC} and M_{ZFC} are deviating from each other, so, we define the temperature below which FC and ZFC magnetizations deviate as the irreversible temperature (T_{irr}), and this is higher than Curie temperature (T_C) for both the samples. **Fig. 4.5**(b) shows the plot of the irreversible magnetizations (the difference between M_{FC} and M_{ZFC}), i.e., $M_{irr} = M_{FC}(T)-M_{ZFC}(T)$ as a function of temperature. This type of difference may be due to the non-homogeneous short-range magnetic ordering, i.e. spin glass cluster. The spin-glass behavior at low-temperatures is discussed in detail in the next section. Both the samples show PM to FM magnetic phase transition near T_C. The Curie temperature T_C, define by the minimum of dM_{ZFC}/dT curve shown in the inset of

Fig. 4.5(b), decreases with doping of Ti^{4+} ions [Hazzez et al. (2016)]. The Curie temperature for the samples $Nd_{0.7}Ba_{0.3}Mn_{1-x}Ti_xO_3$ manganites with x = 0.40 and 0.50 are found to be 30.64 K and 20.17 K, respectively. The peak value of the magnetization decreases with increasing the doping concentration of the Ti^{4+}-ions due to the non-magnetic nature of Ti^{4+}-ions.

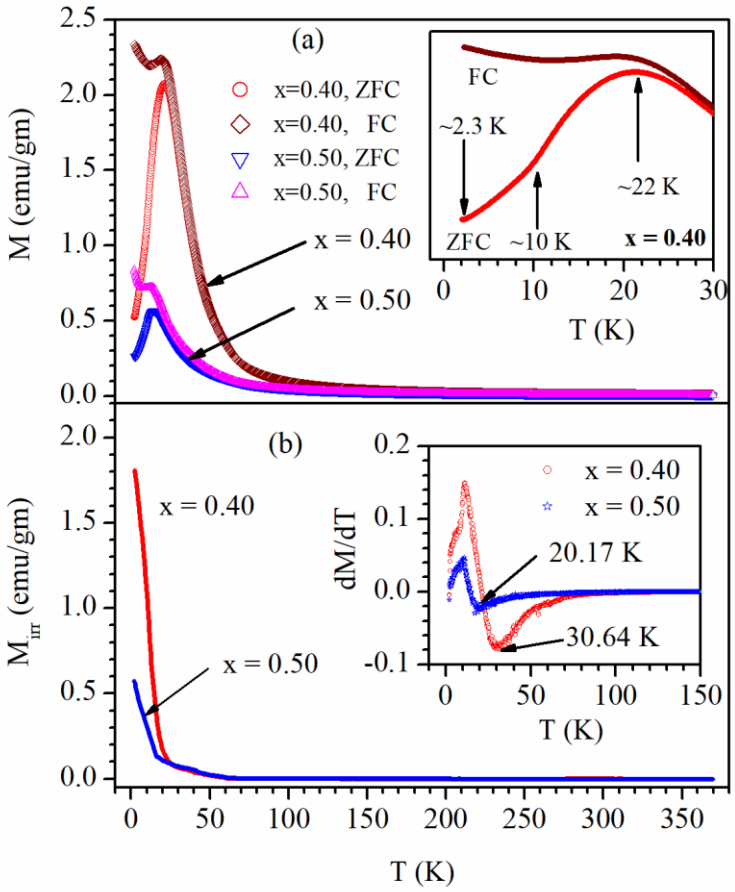

Figure 4.5: (a) The temperature dependence of zero field cooled M_{ZFC} and field cooled M_{FC} magnetization of $Nd_{0.7}Ba_{0.3}Mn_{1-x}Ti_xO_3$ (x = 0.40, 0.50). Inset to (a) shows zoomed view of M(T) curves at low-temperatures for x = 0.40. (b) The difference between M_{FC} magnetization and M_{ZFC} as a function of temperature. Inset shows the temperature dependence of derivative dM_{ZFC}/dT curves for $Nd_{0.7}Ba_{0.3}Mn_{1-x}Ti_xO_3$ (x = 0.40, 0.50).

4.3.2.2. Temperature Dependent Inverse dc Susceptibility Studies

The temperature dependence of inverse dc susceptibility measured in ZFC mode at a constant field of 200 Oe for $Nd_{0.7}Ba_{0.3}Mn_{1-x}Ti_xO_3$ (x = 0.40, 0.50) is shown in **Fig. 4.6**. In the high-temperature paramagnetic region, inverse susceptibility shows linear behavior, obeys Curie-Weiss law, $\chi^{-1} = (T-\theta_{CW})/C$, where C and θ_{CW} are Curie-Weiss constant and Curie-Weiss temperature, respectively. The value of θ_{CW} are found to be 74.02 and 62.07 K for x = 0.40 and 0.50, respectively. The positive valve of θ_{CW} confirms the presence of PM to FM phase transition. The value of Curie-Weiss constant (C) decreases with the increase of Ti^{4+}-ions and results in decrease of magnetization for higher doping level. The effective experimental paramagnetic moment calculated using the expression: $\mu_{eff}^{exp}(\mu_B) = \sqrt{8C}$, comes to be 5.64 and 4.55 μ_B for the samples with x = 0.40 and 0.50, respectively [Kundu et al. (2013)]. The value of the theoretical effective paramagnetic magnetic moment calculated by the relation (4.1) is given below:

$$\mu_{eff}^{theo}(\mu_B) = \sqrt{0.7\mu_{eff}^2(Nd^{3+}) + (0.7-2x)\mu_{eff}^2(Mn^{3+}) + (x-0.3)\mu_{eff}^2(Mn^{2+})} \quad (4.1)$$

The theoretical values of the effective paramagnetic moment are found to be 4.97 and 4.84 μ_B for the samples with x = 0.40 and 0.50, respectively. The value of $\mu_{eff}^{exp}(\mu_B)$ is found to be higher than the value of $\mu_{eff}^{theo}(\mu_B)$ for the sample with x = 0.40 due to the presence of inhomogeneous phase in the paramagnetic region [Phong et al. (2016a)]. The values of Curie temperature (T_C), Curie-Weiss temperature (θ_{CW}), Curie-Weiss constant (C), effective values of the experimental and theoretical paramagnetic moment are given in **Table 4.2**.

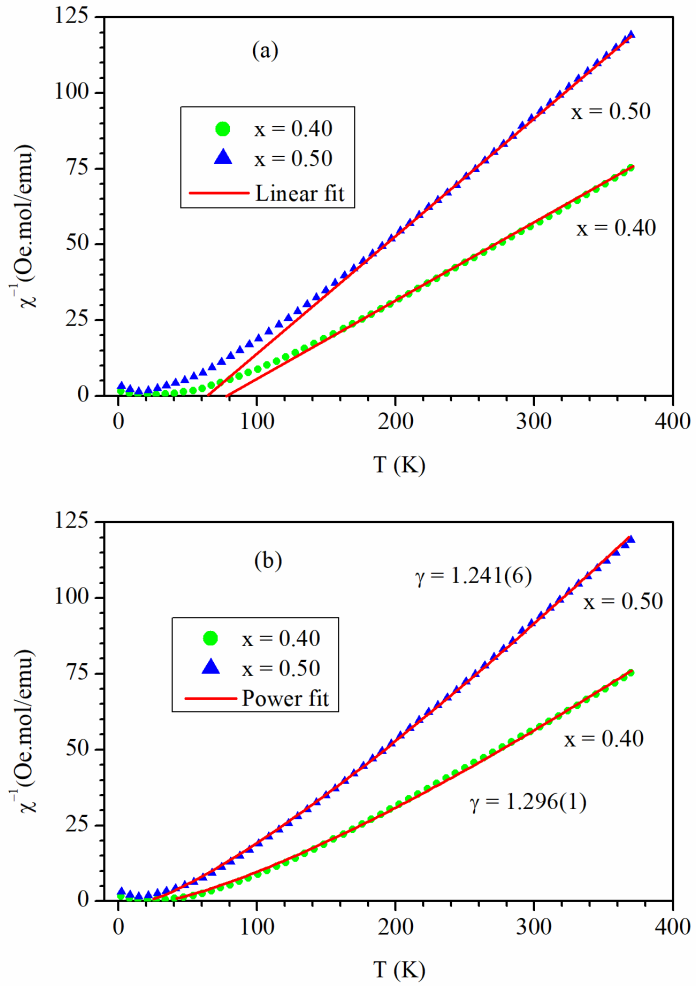

Figure 4.6: (a) and (b) **T**emperature dependence of dc inverse susceptibility of $Nd_{0.7}Ba_{0.3}Mn_{1-x}Ti_xO_3$ (x = 0.40, 0.50) in ZFC mode showing PM-FM phase transition near T_C. The straight line Curie-Weiss fit to experimental data is shown in (a) while (b) shows fits using power law.

The critical exponent (γ) for the magnetic susceptibility for both the samples were estimated using the power relation: $\chi_m^{-1} = A|T - T_C|^{\gamma}$, where A is a proportionality constant [Chaikin et al. (2000); Kumar et al. (2019)]. **Fig. 4.6**(b) demonstrates experimental and fitted curves using the above power relation for inverse susceptibility. The value of the critical exponent of magnetic susceptibility decreases with increasing Ti-doping concentration. The value of magnetic susceptibility critical exponents (γ) is 1.296(1) and 1.241(6) for x = 0.40 and 0.50, respectively. The

estimation of the value of γ suggests that the nature of magnetic interactions is very close to the ideal 3D-Ising model. In general, the value of γ is of the order 1.241 for typical 3D-Ising systems where critical fluctuations are essential [Chaikin et al. (2000); Baazaoui et al. (2016)].

Table 4.2: Curie temperature (T_C), Curie-Weiss temperature (θ_{CW}), Curie constant (C), theoretical and experimental values of the effective paramagnetic moments(μ_{eff}^{theo}) (μ_{eff}^{exp}), coercive field (H_C) and remnant magnetization (M_r) for $Nd_{0.7}Ba_{0.3}Mn_{1-x}Ti_xO_3$ with x = 0.40 and 0.50.

x	T_C (K)	θ_{CW} (K)	C(emu.K/ Oe.mol)	μ_{eff}^{exp} (μ_B)	μ_{eff}^{theo} (μ_B)	H_C (Oe)	M_r (emu/gm)
0.40	30.64	74.02	3.98	5.64	4.97	156.59	1.28
0.50	20.17	62.07	2.58	4.55	4.84	61.74	0.20

4.3.2.3. Field Dependent Magnetization Studies

The field dependence of the magnetization M(H) curve for $Nd_{0.7}Ba_{0.3}Mn_{1-x}Ti_xO_3$ with x = 0.40 and 0.50 measured in ZFC mode at 10 K in the field range of -60 kOe ≤ H ≤ +60 kOe is shown in **Fig. 4.7.** The field dependent magnetization increases slowly for both the samples and remains unsaturated even at the high field of ±60 kOe. The non-saturating nature of the magnetization is due to the presence of some fraction of antiferromagnetic (AFM) phase. The maximum magnetization at 60 kOe are 51.09 emu/gm and 35.93 emu/gm for x = 0.40 and x = 0.50, respectively. The coercive field H_C and remnant magnetization M_r, show drastic change from 156.59 Oe to 61.74 Oe and from 1.28 emu/gm to 0.20 emu/gm, respectively for x = 0.40 and x = 0.50, respectively. **Fig. 4.7**(b) shows isothermal Arrott's plots for the NBMTO samples with x = 0.40 and

0.50. According to the Banerjee's criterion, both the samples exhibit first-order magnetic transition with long-range AFM ordering [Banerjee (1964)].

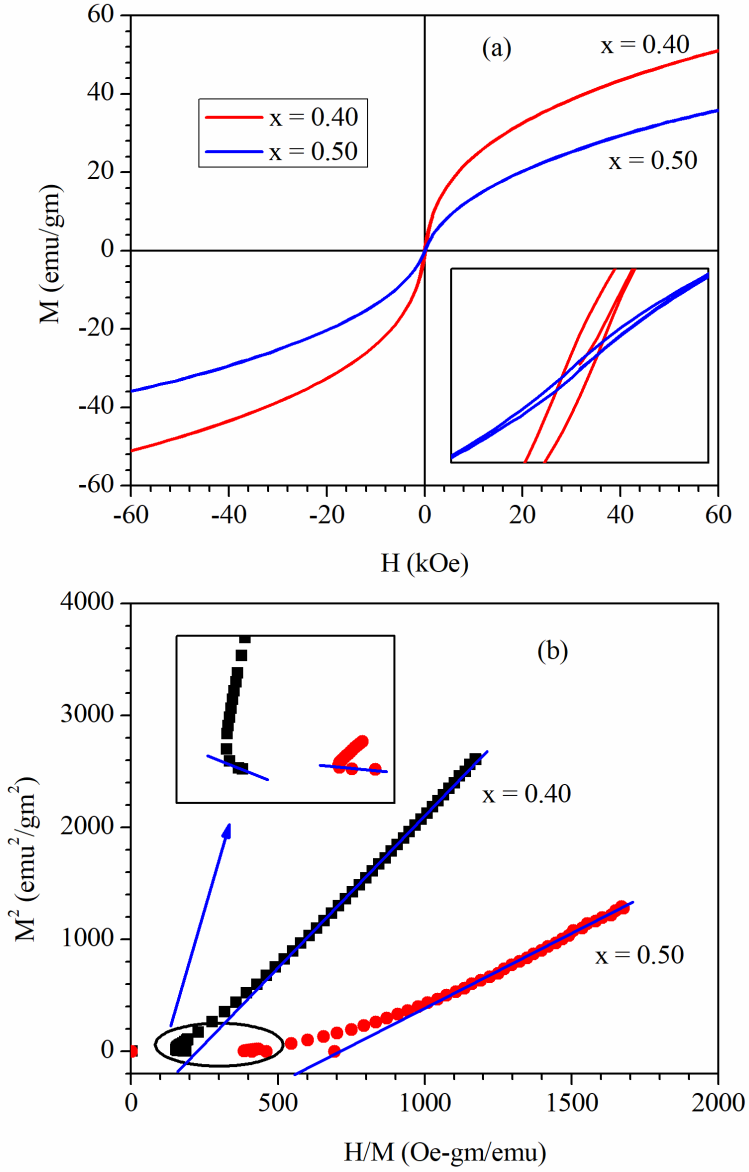

Figure 4.7: (a) The field dependence of magnetization M(H) of $Nd_{0.7}Ba_{0.3}Mn_{1-x}Ti_xO_3$ (x = 0.40, 0.50) in ZFC mode at 10 K in the magnetic field of -60 kOe ≤ H ≤ +60 kOe. The inset of (a) shows the enlarged view of M(H) curves. (b) Isothermal Arrott's plots (M^2 vs. H/M). Inset of (b) shows the enlarged view of M^2 vs. H/M curves.

4.3.2.4. Temperature Dependent ac Susceptibility Studies

The temperature dependence of in-phase $\chi'_{ac}(T)$ and out-phase $\chi''_{ac}(T)$ components of ac-susceptibility for $Nd_{0.7}Ba_{0.3}Mn_{1-x}Ti_xO_3$ with x = 0.40 and x = 0.50 are shown in **Fig. 4.8** in the temperature range of 2 K ≤ x ≤ 150 K. The behavoirs of the $\chi'_{ac}(T)$ for both the samples are very similar to the $\chi_{dc}(T)$ and displays a broad frequency dependent maxima, which shifted towards higher temperature side with increasing frequency as shown in the inset of the **Fig 4.8**.

The peak value of the maxima in $\chi'_{ac}(T)$ decreases while in $\chi''_{ac}(T)$ increases with the increase in measurement frequency as shown in **Fig. 4.8**. These features are reminiscent of frustration of the long-range FM state, commonly referred to as spin-glass [Dho et al. (2002)]. The maxima peak in the $\chi'_{ac}(T)$ or $\chi''_{ac}(T)$ may be referred as the spin-glass freezing temperature (T_f) for a given frequency as discussed in chapter 1, e.g., at f = 100 Hz, T_f = 23.70 K and 15.39 K for x = 0.40 and x = 0.50, respectively. The maxima on the $\chi'_{ac}(T)$ and $\chi''_{ac}(T)$ curves occur at different temperatures, as the peak in $\chi''_{ac}(T)$ curve at f = 100 Hz correspond to T_f = 20.45 K for x = 0.40 and T_f = 13.18 K for x = 0.50. Additionally, the maxima in $\chi'_{ac}(T)$ are rounded while the maxima in $\chi''_{ac}(T)$ are like a cusp. All these features show that these samples do not behave like canonical spin glass but rather as a reentrant spin-glass [Belik et al. (2007)]. The reentrant spin-glass (RSG) behavior has been found in various types of disordered magnetic materials in which there is a competition between long-range FM ordering and spin-glass. As discussed earlier also, the systems in which there is a majority of FM couplings between the individual spins and a sufficiently large number of AFM couplings to create considerable frustration [Kameli et al. (2009)]. The $\chi''_{ac}(T)$ curves for both the samples are qualitatively similar to each other. The $\chi''_{ac}(T)$ exhibits four anomalies below 100 K temperature, first anomaly occurring around 57 K (x = 0.40)

and 45 K (x = 0.50) may correspond to charge ordering transition (T_{CO}), the second anomaly occurring at T_f corresponds to the SG freezing temperature, the third anomaly at around 10 K (T_{Nd}) corresponds to partial FM ordering of Nd-moments with Mn-ions, while the fourth anomaly near 2 K corresponds to any unknown transition and is a subject matter of further study in future [Aslibeiki et al. (2009)].

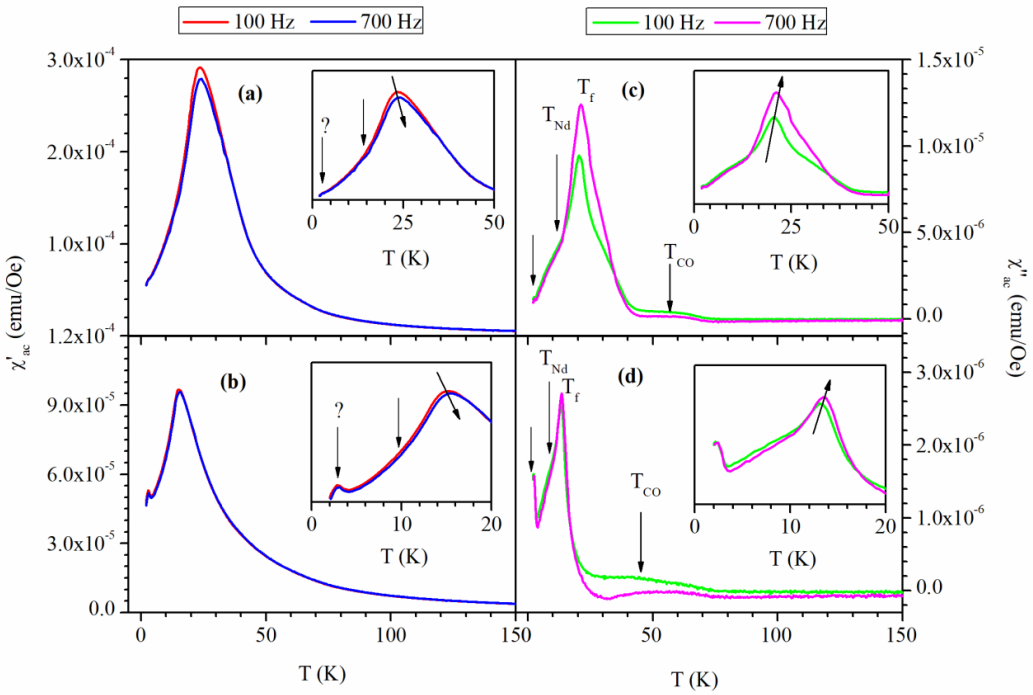

Figure 4.8: Temperature dependence of in-phase part ac susceptibility $\chi'_{ac}(T)$ of $Nd_{0.7}Ba_{0.3}Mn_{1-x}Ti_xO_3$ for (a) x = 0.40 and (b) x = 0.50 measured during cooling with ac field at 100 Hz and 700 Hz. The respective insets show the enlarged view of $\chi'_{ac}(T)$ of ac susceptibility. The temperature dependence of out of phase part ac susceptibility $\chi''_{ac}(T)$ of $Nd_{0.7}Ba_{0.3}Mn_{1-x}Ti_xO_3$ for (c) x = 0.40 and (d) x = 0.50 measured during cooling with ac field at 100 Hz and 700 Hz. The respective insets show the enlarged view of $\chi''_{ac}(T)$ of ac susceptibility.

4.3.3. Dielectric Properties

The temperature dependence of electrical resistivity and electrical conductivity of both samples measured at different frequencies are shown in **Figs. 4.9**(a-b) and (c-d)

for $Nd_{0.7}Ba_{0.3}Mn_{1-x}Ti_xO_3$ manganites with x = 0.40 and 0.50, respectively. The resistivity of the samples decreases with increasing frequency and temperature. The resistivity of the sample with x = 0.50 is almost six times higher than the sample with x = 0.40 at 25°C (RT) and 100 Hz, i.e., resistivity increases with increasing doping concentration of Ti^{4+} ions at Mn-site. The order of electrical resistivity in low and high-temperature regions reveals that both the samples undergo semiconducting to the semi-metallic phase transition. In contrast to the electrical resistivity, electrical conductivity increases with increasing temperature and frequency and exhibits maxima in high temperature, which shifts towards higher temperature side with enhancing Ti^{4+}-doping concentration.

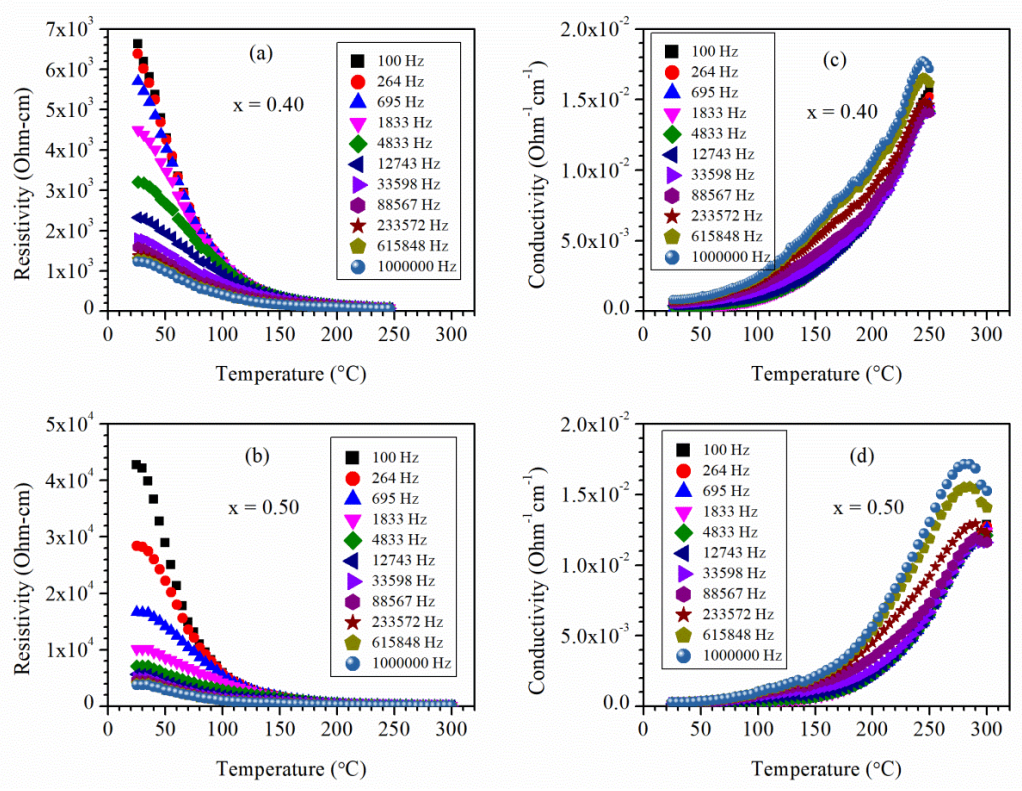

Figure 4.9: Variation of temperature dependent resistivity (a-b) and conductivity (c-d) for $Nd_{0.7}Ba_{0.3}Mn_{1-x}Ti_xO_3$ perovskites with x = 0.40 and x = 0.50, respectively.

The dielectric behavior of the samples was studied in terms of temperature dependence of dielectric permittivity. The dielectric permittivity (k or ε_r) was calculated using Equation (4.2):

$$k = \varepsilon_r = C_p d/\varepsilon_0 A \quad (4.2)$$

Where, C_p, d and A are parallel plate capacitance, thickness, and area of the pellet (capacitor) of the sample. ε_0 is permittivity of the free space equal to 8.854×10^{-14} Farads/cm. The dielectric constant is a ratio of the permittivity of a material to the permittivity of free space ($\varepsilon_r = k = \varepsilon/\varepsilon_0$) also known as relative permittivity of the substance. Frequency and temperature dependence of dielectric constant for $Nd_{0.7}Ba_{0.3}Mn_{1-x}Ti_xO_3$ manganites with x = 0.40 and x = 0.50 is shown in **Figs. 4.9**(a-b), respectively. The value of the dielectric constant in the low-frequency region decreases with increasing temperature, but in higher frequency region it increases with increase in temperature. Both the samples exhibit very high dielectric constant at room temperature of the order of $\sim10^5$. Munoz et al. also observed such a high value of dielectric constant in $Bi_{1-x}Sr_xMnO_3$ manganites with x = 0.40 and 0.50 [Munoz et al. (2009)]. The sample with x = 0.40 shows negative dielectric constant above 150°C temperature and below 10 kHz frequency as shown in the inset of **Fig. 4.10**(a) which is an artifact due to higher conductivity losses. However, the sample with x = 0.50 does not exhibit negative dielectric constant.

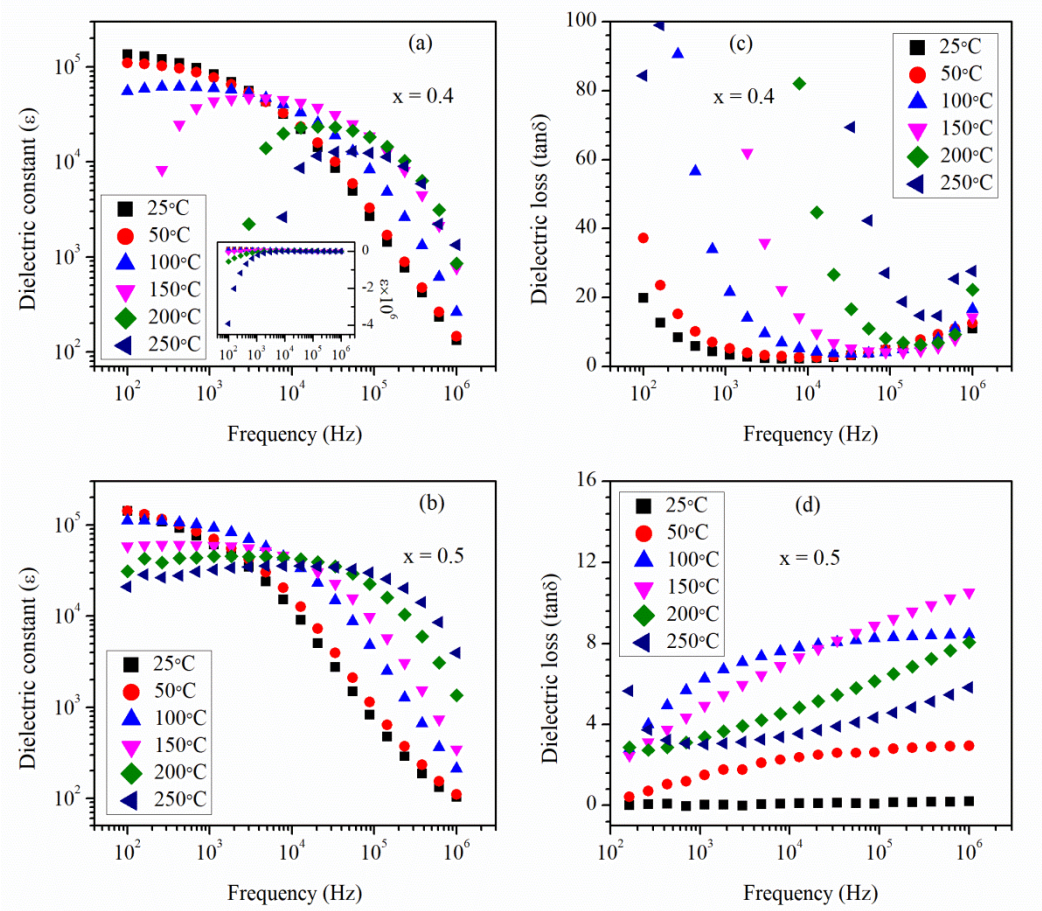

Figure 4.10: Variation of frequency dependent dielectric constant (a-b) and dielectric loss (c-d) for $Nd_{0.7}Ba_{0.3}Mn_{1-x}Ti_xO_3$ manganites with x = 0.40 and x = 0.50, respectively. Inset of (a) shows artifact due to high conductivity losses giving negative dielectric constant for x = 0.40.

Figs. 4.10(c-d) display dissipation factor or dielectric loss (tanδ) for the $Nd_{0.7}Ba_{0.3}Mn_{1-x}Ti_xO_3$ perovskites with x = 0.40 and x = 0.50, respectively as a function of frequency obtained at various temperatures. For $Nd_{0.7}Ba_{0.3}Mn_{0.6}Ti_{0.4}O_3$ sample, we observed very high dielectric loss on and above 100°C. However, the sample $Nd_{0.7}Ba_{0.3}Mn_{0.5}Ti_{0.5}O_3$ manganite shows a very small dielectric loss as compared to the sample of $Nd_{0.7}Ba_{0.3}Mn_{0.6}Ti_{0.4}O_3$ manganite. The room temperature dielectric loss for $Nd_{0.7}Ba_{0.3}Mn_{0.5}Ti_{0.5}O_3$ perovskite is less than unity and remains almost constant. Thus, the Ti^{4+} half-doped $Nd_{0.7}Ba_{0.3}Mn_{0.5}Ti_{0.5}O_3$ manganite is more suitable for technical

applications from the dielectric loss point of view. The occurrence of high dielectric loss for the sample with x = 0.40 is due to more conduction electrons at higher temperatures and low-frequency region. Thakur et al. (2013) also reported very high dielectric loss up to the order of ~10^4 for $Bi_{1-x}Sr_xMnO_3$ (BSMO) manganites with $0.40 \leq x \leq 0.55$ usually in the low-frequency region and at high temperature. They suggested that the dielectric losses in BSMO manganites are due to the conductivity losses in the samples.

4.4. Conclusions

The polycrystalline samples of $Nd_{0.7}Ba_{0.3}Mn_{1-x}Ti_xO_3$ (x = 0.40 and 0.50) perovskite manganites have been synthesized using auto-combustion method. The structural, magnetic and dielectric properties of these manganites were investigated in detail using X-ray diffraction, magnetic measurements, and impedance measurements, respectively. HR-SEM and EDS were used to study microstructures and elemental compositions. Analysis of the HR-SEM micrographs reveals that the samples with x = 0.40 and 0.50 exhibit microflakes and microrods in microstructures, respectively. The Rietveld structure refinement using X-ray diffraction patterns confirms the coexistence of two crystallographic phases of tetragonal structures with *I*4*/mcm* and *P*4*mm* space groups, in both the compositions. The temperature dependent magnetization measurement reveals that these samples exhibit paramagnetic to ferromagnetic phase transition at characteristic Curie temperature (T_C). The value of T_C reduces with increasing doping level of Ti^{4+}-ions as a result of deteriorating double exchange interaction. The zero field cooled, and field cooled magnetization plots at lower temperatures deviate from each other. The significant difference between these curves shows the possibility of the existence of non-equilibrium spin-glass cluster behavior in these manganites. The non-equilibrium low-temperature behavior of the samples was

investigated using ac-susceptibility measurements. The ac-susceptibility data analysis reveals that these samples are not showing conventional spin glass behavior but they are exhibiting reentrant spin glass (RSG) state. The field dependent magnetization measurements show the coexistence of ferromagnetic and antiferromagnetic components for both the systems. The impedance spectroscopy measurements reveals that the resistivity of the manganites increases and dielectric loss decreases with increasing Ti^{4+}-ions concentration and they display very high dielectric constant of the order of 10^5.